AGU ADVANCING EARTH AND SPACE SCIENCES

AGU Advances

RESEARCH ARTICLE
10.1029/2025AV002030

Mechanisms of Surface Meltwater Ponding and Drainage on the Greenland Ice Sheet Revealed Using SkySat Imagery and Deep Learning

J. C. Ryan[1], **R. T. Datta**[2], **and S. W. Cooley**[1]

[1]Division of Earth and Climate Sciences, Nicholas School of the Environment, Duke University, Durham, NC, USA, [2]Department of Geoscience and Remote Sensing, TU Delft, Delft, The Netherlands

Peer Review The peer review history for this article is available as a PDF in the Supporting Information.

Key Points:

- We use deep learning to classify surface meltwater on the Greenland Ice Sheet with higher accuracy than conventional approaches
- We find that small water features (<0.015 km^2) account for a substantial fraction of surface water area during May and August
- We show that synchronous filling and drainage of seven lakes in our study site is facilitated by the development of supraglacial rivers

Supporting Information:

Supporting Information may be found in the online version of this article.

Correspondence to:

J. C. Ryan,
jonathan.ryan@duke.edu

Citation:

Ryan, J. C., Datta, R. T., & Cooley, S. W. (2026). Mechanisms of surface meltwater ponding and drainage on the Greenland Ice Sheet revealed using SkySat imagery and deep learning. *AGU Advances*, *7*, e2025AV002030. https://doi.org/10.1029/2025AV002030

Received 13 AUG 2025
Accepted 19 DEC 2025

Author Contributions:

Conceptualization: J. C. Ryan
Data curation: J. C. Ryan
Formal analysis: J. C. Ryan
Funding acquisition: J. C. Ryan, R. T. Datta, S. W. Cooley
Investigation: J. C. Ryan
Methodology: J. C. Ryan, S. W. Cooley
Visualization: J. C. Ryan
Writing – original draft: J. C. Ryan
Writing – review & editing: J. C. Ryan, R. T. Datta, S. W. Cooley

Abstract Surface meltwater impacts Greenland Ice Sheet mass balance indirectly by reducing albedo and promoting hydrofracture. However, fully understanding both processes requires accurate mapping of small-scale features such as ponds, channels, and moulins that govern meltwater formation and drainage. Here we investigate surface water dynamics at high spatial (~1 m) and temporal resolution by applying deep learning to high-resolution imagery from the SkySat constellation. We develop a U-Net model that robustly classifies surface meltwater with higher accuracy than a conventional thresholding approach. Our mapping reveals that small water features (<0.015 km^2) account for a substantial fraction of surface water area in the western Greenland Ice Sheet ablation zone, especially during May (67%) and August (38%). However, we find that seasonal variability in surface water area is primarily driven by the filling and draining of 12 large supraglacial lakes. The high spatial resolution of the SkySat imagery reveals that much of this variability can be attributed to the development of narrow supraglacial channels that facilitate the drainage of upstream lakes into a single downstream lake. When the downstream lake rapidly drains, we observe synchronous lake drainage across our study site between 13–16 June. This cascading drainage event explains how lakes drain even when they are situated in compressive ice flow regimes and provides an alternative mechanism for synchronous lake drainages typically attributed to transmission of stress perturbations. Our study demonstrates that deep learning applied to high-resolution satellite imagery can provide valuable insights into supraglacial hydrology.

Plain Language Summary Meltwater produced by the Greenland Ice Sheet is a major contributor to sea-level rise. But, before it flows into the ocean, meltwater can further increase ice sheet mass loss by (a) reducing surface albedo, which increases solar energy absorption, and (b) weakening glaciers and ice shelves, which enhances iceberg production. Understanding both processes requires detailed maps of small water features, such as ponds, streams, and moulins that are difficult to detect with standard satellite imagery. In this study, we applied a deep learning model (U-Net) to map surface meltwater in high-resolution SkySat images. We found that small water features account for a substantial fraction of surface water area, especially in May and August. However, most seasonal variation in meltwater coverage is driven by the filling and draining of 12 large supraglacial lakes. The high-resolution SkySat images reveal that many of these lakes drain simultaneously through a previously undocumented mechanism that begins when several upstream lakes drain into a single downstream lake via narrow supraglacial channels. When the downstream lake drains rapidly, it triggers drainage of the entire connected system. This work shows that combining deep learning with high-resolution satellite images can enhance our understanding of ice sheet meltwater dynamics.

1. Introduction

Every summer, a large amount of meltwater is produced on the surface of the Greenland Ice Sheet in the form of supraglacial lakes, streams, and ponded crevasses (Chudley et al., 2021; Smith et al., 2015; Zhang et al., 2023). Surface meltwater in these features can enhance ice sheet mass loss in several ways. Ponded meltwater can reduce ice sheet surface albedo, leading to higher rates of shortwave energy absorption, causing melt rates that are 110%–170% higher than nearby non-inundated ice sheet surfaces (Lüthje et al., 2006; Tedesco et al., 2012). Likewise, meltwater can cause fractures to propagate much deeper than they otherwise would (Alley et al., 2005; Chandler & Hubbard, 2023). This process, termed "hydrofracture," can drive fracture propagation to the ice-sheet bed, pressurizing the subglacial drainage system, causing enhanced seasonal ice flow (Das et al., 2008; Schoof, 2010; Van De Wal et al., 2008). In warmer summers, the area of surface meltwater increases (Glen

et al., 2025; Rawlins et al., 2023; Zhang et al., 2023), which has the potential to further reduce albedo and initiate hydrofracture at higher elevations of the ice sheet. Constraining feedbacks between climate warming, ice dynamics, and surface meltwater is therefore imperative for accurately forecasting Greenland Ice Sheet mass loss.

Most studies investigate surface meltwater coverage and drainage using medium-resolution (10–30 m) satellite imagery provided by Landsat 8/9 or Sentinel-2A/B. These studies have documented large seasonal and interannual variability in surface meltwater area at individual glacier (Macdonald et al., 2018; Wang & Sugiyama, 2024), regional (Glen et al., 2025; Lutz et al., 2023; Rawlins et al., 2023; Turton et al., 2021; Williamson et al., 2018; K. Yang et al., 2019; K. Yang et al., 2021) and ice-sheet scales (Dunmire et al., 2025; Fan et al., 2025; Hu et al., 2021; Zhang et al., 2023). However, the spatial resolution of Landsat 8/9 and Sentinel-2A/B may struggle to resolve small ponds (e.g., <1,000 m^2), narrow channels (<10 m), and moulins, obscuring complete understanding of the impact of surface meltwater on ice sheet mass balance. Small water features (<1,000 m^2), for example, accounted for 64% of the total surface water area in the upper ablation zone of the western Greenland Ice Sheet on 21 July (Ryan et al., 2025). Excluding these small water features therefore limits deeper investigation into the albedo-lowering effect caused by surface meltwater. Similarly, evidence of narrow channels and moulins can be used to determine mechanisms of supraglacial lake drainage (Poinar & Andrews, 2021). For example, drainage through a moulin in the lakebed (i.e., "bottom drainage") provides evidence of full-depth hydrofracture that rapidly pressurizes the subglacial system with immediate impacts on ice flow (Das et al., 2008; Doyle et al., 2013; Stevens et al., 2015). Alternatively, drainage caused by a lake breaching the local basin into a pre-existing moulin (i.e., "overspill drainage") is a slower process that does not require full-depth hydrofracture and has a more muted impact on ice flow (Kingslake et al., 2015; Stevens et al., 2024; Tedesco et al., 2013). The coupling between ice flow and supraglacial lake drainage can therefore only be fully understood by considering drainage mechanisms.

High-resolution drone and satellite imagery provides more opportunities for robustly mapping small water features and supraglacial lake drainage mechanisms. Ryan et al. (2018), for example, mapped surface meltwater using drone imagery with a spatial resolution of 15 cm over a 15 km^2 transect across the western Greenland ablation area. Smith et al. (2017) mapped surface meltwater using WorldView-2 and WorldView-3 images with a spatial resolution of 2 m over a 63.1 km^2 area in a similar sector of the ice sheet. However, while drone and WorldView imagery offer high spatial resolution mapping capabilities, logistical and tasking constraints have prevented systematic mapping of surface meltwater dynamics at both high spatial and high temporal resolution. An alternative source of high-spatiotemporal-resolution imagery may be provided by constellations of small, low-cost imaging satellites known as "SmallSats" or "CubeSats." For example, Planet (formerly Planet Labs, Inc.) operates the SkySat-C constellation which consists of 19 SmallSats (110 kg) launched between 2016 and 2020 (Jacobsen, 2022). The SkySat-C satellites have multispectral cameras that can acquire imagery with spatial resolution of 0.75–1 m. Furthermore, these satellites can be tasked to collect imagery with rapid revisit times (i.e., sub-daily) over a specific regions-of-interest (Bhushan et al., 2021). SkySat satellites therefore have several advantages over traditional medium-resolution platforms such as Sentinel-2 and Landsat. Yet while SkySat has been used to derive depths of several supraglacial lakes in western Greenland (Datta & Wouters, 2021), it has not been used for systematically mapping surface meltwater coverage and drainage.

Mapping surface meltwater using SkySat (or other CubeSat) constellations is challenging because imagery is acquired by different sensors, at different times of the day, and at different satellite elevation angles. Image classification techniques that assume consistent solar and satellite geometries (i.e., global thresholding) may therefore not be appropriate (e.g., Glen et al., 2025; Rawlins et al., 2023). On the other hand, scene-specific thresholding may also be unfeasible given the large number of images collected by multiple satellites operating in a constellation (e.g., Zhang et al., 2023). New approaches are therefore required to classify imagery from satellite constellations. One option that is gaining popularity is the use of deep learning (Shen, 2018). In particular, convolutional networks (CNs), a type of deep learning algorithm, can learn features directly from images by combining convolutional and pooling layers. Studies that have applied CNs for water segmentation from satellite imagery report superior accuracy and generalizability compared to pixel-based approaches (Wieland & Martinis, 2019; Wieland et al., 2023; Yuan et al., 2020). For example, Lutz et al. (2023) demonstrated that a CN was better at detecting small supraglacial lakes in Sentinel-2 imagery than a global thresholding approach. The potential of CNs for mapping surface water from SkySat imagery, however, has yet to be explored.

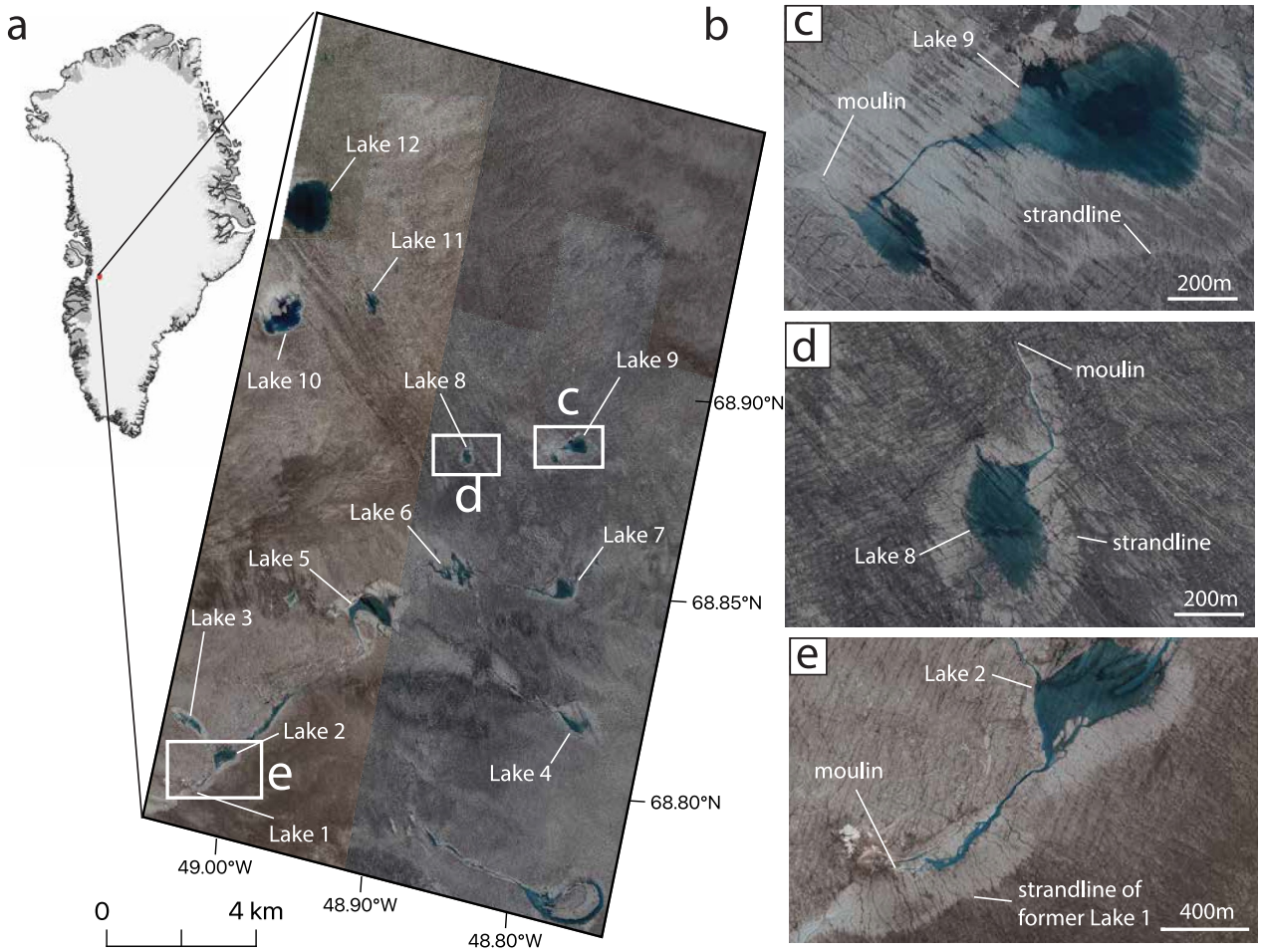

Figure 1. Map of study site on the Greenland Ice Sheet. (a) Location of study site in Greenland. (b) True color composite of SkySat imagery (RGB) from July 2019 showing study site with the 12 supraglacial lake labeled. (c)–(e) Moulins, supraglacial channels, and strandlines of former lake levels can be easily identified in the high-resolution SkySat imagery. @ Planet Labs PBC 2025. All rights reserved.

Here we investigate the full seasonal cycle of surface meltwater ponding and drainage on the Greenland Ice Sheet at high spatial and temporal resolution by applying deep learning techniques to imagery acquired by the SkySat constellation. To do this, we develop a U-Net, a type of CN developed for semantic segmentation, to accurately classify meltwater on the surface of the ice sheet. We apply the U-Net to track changes in surface meltwater area across a 300 km^2 study site in the western ablation zone from 2 May–30 August 2019. Our automated mapping allows us to investigate mechanisms of meltwater ponding, that occurs between May and early June, and mechanisms of meltwater drainage, that occurs rapidly during June and then more steadily throughout the rest of the summer. Unlike previous studies that rely on medium-resolution satellite imagery, our mapping resolves small water features, such as ponds and streams, enabling more accurate quantification of the radiative effect caused by surface meltwater ponding. Likewise, our use of high-resolution imagery provides evidence for distinct styles of lake drainage, enabling insight into the causes of synchronous and asynchronous lake drainage at our study site. Overall, our study advances the use of deep learning and tasked high-resolution commercial satellite imagery for characterizing different mechanisms of supraglacial lake drainage on the Greenland Ice Sheet.

2. Data

2.1. Study Site

We investigated surface meltwater at a ~300 km^2 study site spanning 1,180–2,200 m a.s.l. of the western Greenland Ice Sheet ablation zone from 68.8 to 69.0°N to 48.7–49.1°W (Figure 1). The choice of our study site was guided by several factors. First, our study site is known to contain many supraglacial lakes, some of which

have been observed to drain rapidly (Cooley & Christoffersen, 2017; Liang et al., 2012; Miles et al., 2017; Morriss et al., 2013). Second, our study site is ∼25 km upstream of the "North Lake Array" (∼1,000 m a.s.l.), a heavily instrumented site that has been used to investigate the coupling between supraglacial hydrology and ice flow (Das et al., 2008; Stevens et al., 2015, 2016, 2024). Third, and most importantly, our study site was imaged regularly by SkySat during the summer of 2019 as part of a larger tasking campaign to collect repeat imagery over multiple regions of the Greenland Ice Sheet concurrently with ICESat-2 and NASA Operation IceBridge (Datta & Wouters, 2021). The combination of supraglacial lake density, previous field research, and image availability at, or in the vicinity of, our study site therefore provides a unique opportunity to assess the potential of high-resolution SkySat imagery for investigating surface meltwater dynamics on the Greenland Ice Sheet.

2.2. Satellite Platform and Imagery

In the summer of 2019, thirteen SkySat-C satellites (SkySat-3–15) were in sun-synchronous orbits at an altitude of 500 km (although they were subsequently lowered to 450 km in early 2020). There are another six SkySat-C satellites (SkySat-16–21) in mid-inclination orbits at an altitude of 400 km which were not used in this study. Each SkySat satellite has three cameras that acquire imagery in a "tuning fork" orientation. Each camera has one detector that acquires multispectral imagery (blue: 450–515 nm, green: 515–595 nm, red: 605–695 nm, and NIR: 740–900 nm) and another that collects panchromatic (450–900 nm) imagery although we did not use panchromatic imagery in our study. The ground footprint of the multispectral detector is ∼2.5 × 1 km, yielding a spatial resolution of ∼1 m at nadir (in 2019). Overlapping images (termed "Scenes") are post-processed to image strips (termed "Collects") that represent ∼60 Scenes with a total ground footprint of ∼25 × 9 km. Planet processes these "Collects" to several different levels. In this study, we used "pansharpened multispectral," "analytic," and "analytic DN" products. All of these products are orthorectified, although only the "analytic" and "analytic DN" products are radiometrically corrected for sensor artifacts. The "analytic" product is also transformed to top-of-atmosphere radiance while the "analytic DN" product represents uncalibrated digital numbers. We manually excluded Collects that contained clouds. In total, we obtained SkySat imagery over our study site 29 times during our 2 May–30 August 2019 study period, equivalent to a mean temporal resolution of 4.1 days.

We supplemented SkySat with imagery from Sentinel-2 so that we could more precisely identify the timing of supraglacial lake drainage. The Sentinel-2 mission consists of two satellites (A and B) that each carry the Multi-Spectral Instrument, which has 13 spectral channels in the visible/near-infrared (VNIR) and shortwave infrared spectral range (SWIR). In this study, we used Level-1C scenes which provide top-of-atmosphere reflectance and the VNIR bands (red, blue, green, and NIR) which have a spatial resolution of 10 m. Sentinel-2 has a much larger swath width than SkySat (290 vs. 9 km), enabling near-daily revisit times at our study site with just two satellites. Combining Sentinel-2 with SkySat therefore enables comprehensive mapping of surface meltwater at both high spatial and temporal resolution.

3. Methods

3.1. Pre-Processing

We prepared our satellite imagery for deep learning by rescaling the original images (which are either 12- or 16-bit) to 8-bits using linear interpolation and resampling them to a common spatial resolution (1 m) and coordinate system (UTM Zone 22N). Next, we used a local thresholding approach to produce labeled (or "ground-truth") maps of surface coverage. To do this, we first used the green and NIR bands to compute a Normalized Differenced Water Index (NDWI) for each image which enables accurate differentiation of surface water from ice and snow (e.g., Rawlins et al., 2023). We then developed a GUI using the OpenCV library in Python that allowed us to manually identify image-specific NDWI thresholds for classifying pixels into "water" versus "non-water" classes. Given the size of the raw images (∼28,000 × 10,000 pixels), we randomly selected 10 subregions (2,000 × 4,000 pixels) in each image for identifying NDWI thresholds. The mean of the NDWI thresholds manually identified from each of these 10 subregions was used to classify the entire image. The output from this step is a classified (i.e., binary) water mask that can be used for training a deep learning algorithm (Figure 2a).

3.2. Training Data Set

We produced a training data set for our deep learning algorithm by sampling our imagery and using a random stratified approach. We opted for a random stratified approach so that we could ensure that our CN was trained on

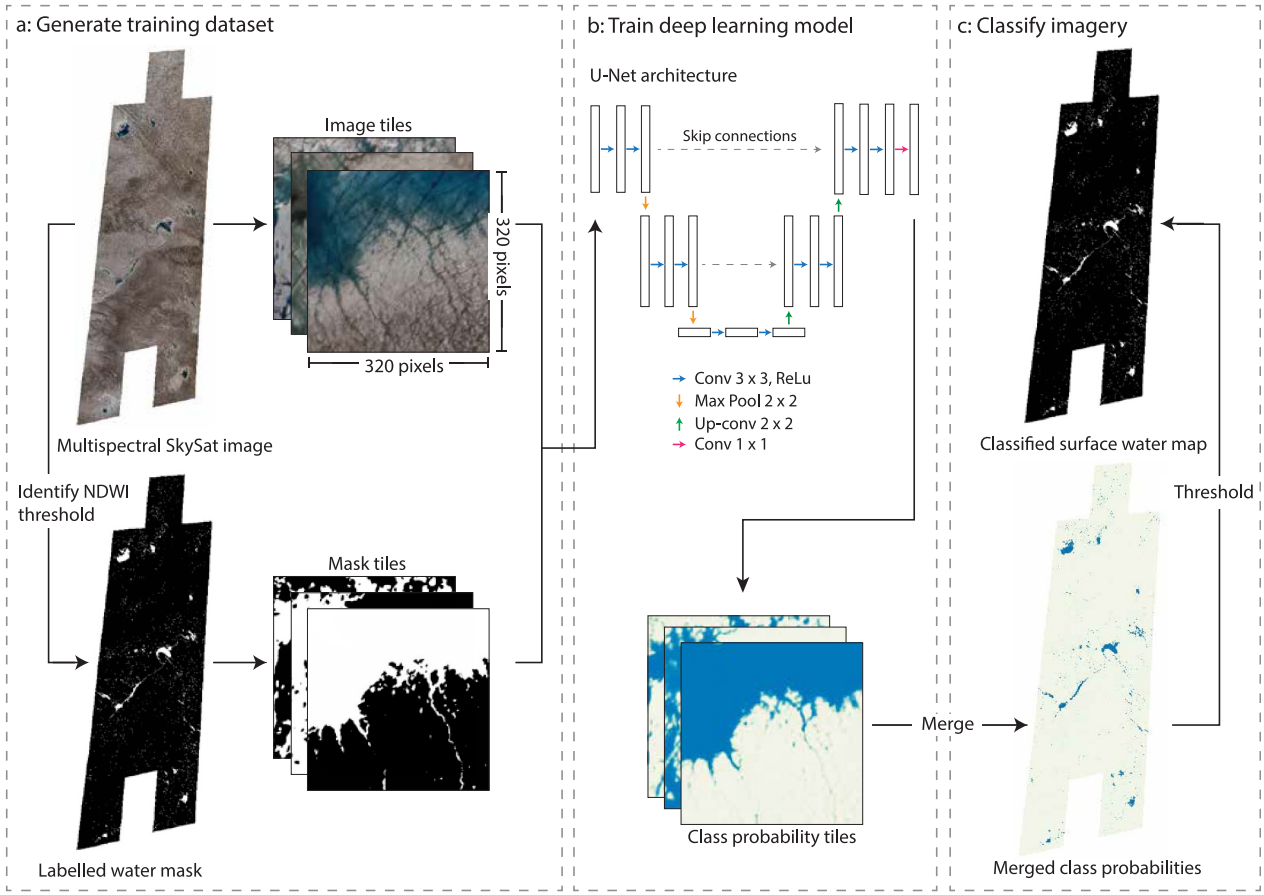

Figure 2. Deep learning approach for classifying surface meltwater in SkySat imagery. (a) We generate a training data set containing by tiling our imagery and producing paired image-mask tiles. (b) We train a U-Net model to predict class probabilities using the training data set. (c) We merge and threshold the class probabilities to product a fully classified SkySat Collect. @ Planet Labs PBC 2025. All rights reserved.

the full range of hydrological conditions at our study site (e.g., meltwater features with different areas, meltwater ponded on snow vs. glacier ice). To do this, we first resampled the labeled water masks to a spatial resolution of 32 m and computed the mean water fraction in each grid cell. We then categorized these grid cells into one of 12 bins based on their water fraction. The edges of the bins were evenly spaced by between 0 and 0.5 (with a width of 0.05) with a final bin for water fractions >0.5. We randomly selected two grid cells within each bin, yielding 22 grid cells per image. The extents of these grid cells were used to select paired image-mask tiles (320 × 320 pixels) within our original (i.e., 1 m spatial resolution) images and water masks (Figure 2a).

Our final training data set consisted of 1,812 paired image-mask tiles. The imagery has four dimensions representing the Red, Green, Blue, and NIR bands. The mask has a single dimension that represents the presence/absence of water for each pixel (Figure 2a). We randomly separated the paired image-mask tiles into training, validation, and testing data sets with a 72/8/20 split. The training data set was used to train the deep learning algorithm, the validation data set was used to log the performance of the model after every training cycle or epoch, and the testing data set, which was "held-out" from the training process, was used to evaluate the final performance of the fully trained model.

3.3. Deep Learning Model

We performed semantic image segmentation using a CN based on the U-Net architecture (Figure 2b) (Ronneberger et al., 2015). The U-Net was originally developed for biomedical imaging but has demonstrated impressive capabilities in environmental remote sensing, including surface water mapping (Wieland & Martinis, 2019). We used a lightweight version of the original U-Net that consists of two encoder and two decoder levels (Figure 2b). Each level of the encoder contains two 3 × 3 convolutional layers with Rectified Linear Unit activation functions,

followed by a 2 × 2 max-pooling layer for spatial downsampling. The number of filters doubles at each level (16 and 32, respectively). A bottleneck layer with 64 filters and a 3 × 3 convolution captures the deepest feature representations. The decoder path mirrors the encoder and performs upsampling using 2 × 2 nearest-neighbor upsampling layers, followed by 3 × 3 convolutional layers. Skip connections concatenate feature maps from the encoder to their corresponding decoder layers, enabling precise localization. The final layer applies a 1 × 1 convolution with a sigmoid activation function to generate a segmentation mask with continuous values between 0 and 1 that represent probabilities of our target class (water). We integrated this U-Net architecture into our deep learning pipeline using TensorFlow 2.19.0. Training was performed using the "Adam" algorithm with a learning rate of 0.001 (Kingma & Ba, 2017), and a binary cross-entropy loss function. We trained the model with batches of 16 paired image-mask tiles for 20 epochs on a Mac Mini with an Apple M2 Pro GPU @ 3.5 GHz and 32 GB RAM.

3.4. Image Classification

Once trained, we applied our U-Net to all SkySat imagery over our study site. This step required dividing the imagery into 320 × 320 tiles, classifying the individual tiles, and merging the tiles back together (Figure 2c). Since the tiles are classified independently, this process can cause artifacts at the borders of tiles (Wieland & Martinis, 2019). We removed these errors by tiling our images with 10% (32 pixels) overlap in both horizontal and vertical directions before prediction. Then, during the merging process, we averaged the class probabilities of overlapping pixels before converting them to a binary water mask using a threshold of 0.5. We also found that valid image pixels that were immediately adjacent to null values (i.e., "edge pixels") were often incorrectly classified (almost always as water). We accounted for these errors by padding edge pixels by three pixels before prediction. The values of the padded pixels were set to the values of the nearest edge pixels of the original image. After prediction, these padded pixels are removed before merging the tiles. We found that these two strategies effectively accounted for border effects during the classification process, allowing us to produce seamless maps of surface water coverage.

We evaluated the performance of our U-Net using our testing data set which includes 363 paired image-mask tiles that were not used during the training process (Figure 3). We computed accuracy, precision, and recall scores to evaluate the overall performance of our approach as well as its ability to distinguish true and false positives. We also investigated the relative accuracy of our deep learning approach by comparing our results to image tiles classified using a global thresholding approach. To define the global threshold, we iterated through a range of NDWI values (from 0 to 0.3 with a 0.01 interval) to find the threshold that provided the highest accuracy for each image-mask tile (i.e., image-specific). We then defined the global threshold as the mean of the image-specific thresholds (NDWI > 0.10). This analysis enabled us to compare our deep learning approach with a more conventional approach for mapping surface water (Fan et al., 2025; Glen et al., 2025; Rawlins et al., 2023; Turton et al., 2021).

3.5. Analysis of Surface Meltwater Feature Area

We identified 12 supraglacial lakes in our study site. In June, these lakes all have mean areas >0.15 km^2 so we used this threshold to differentiate these water features from other water features in our study site. To track the changes in the area of these lakes, we manually digitized polygons around each lake, labeled clusters of water pixels within these polygons with unique identifiers (8-neighbor pixel connectivity), and computed the area of the largest water feature. This clustering approach allowed us to exclude small water features contained within the polygons that were not connected to the main supraglacial lake. We note that the digitized polygons extend ∼500 m beyond the maximum perimeters of the lakes to account for georeferencing errors in SkySat imagery. Therefore, we also excluded water pixels outside of the polygons, even if they were connected to the main supraglacial lake. To more precisely identify the timing of lake drainage, we quantified supraglacial lake area using Sentinel-2 imagery. To do this, we computed a Normalized Difference Water Index (NDWI) index using the green (band 3) and NIR bands (band 8). We then classified water using a global threshold of 0.20 and computed the area of each supraglacial lake using the approach we developed for the SkySat imagery.

We investigated the dynamics of surface water not contained in supraglacial lakes using a similar labeling approach. To do this, we first labeled clusters of water pixels (8-neighbor pixel connectivity) and computed the area of each water feature. We then computed the fraction of water contained in the following size classes: <15,000, >15,000 and <50,000, >50,000 and <150,000, and >150,000 m^2. The first three categories would be

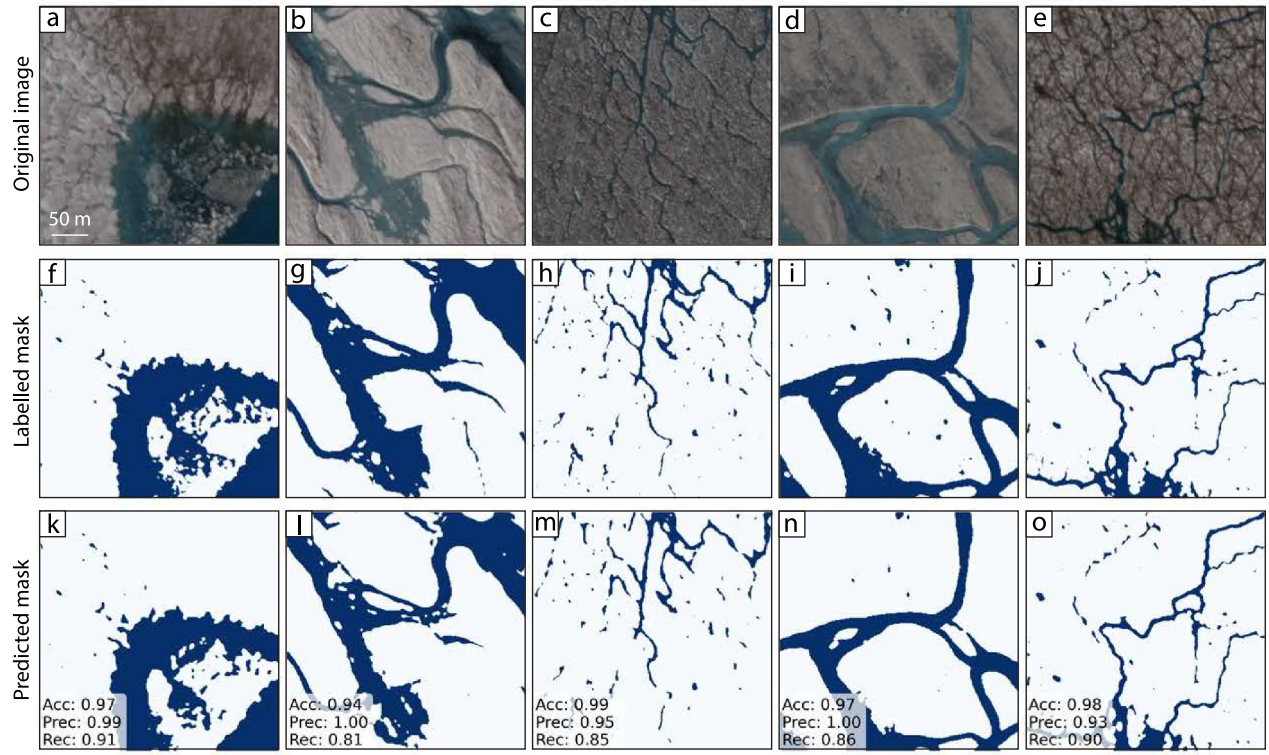

Figure 3. Sample of tiles demonstrating results of semantic segmentation of surface water. (a)–(e) Image tiles (320 × 320 m) displayed as RGB. (f)–(j) Labeled surface water masks used for training and evaluation of U-Net. (k)–(o) Predicted surface water masks with corresponding accuracy, recall, and precision scores.

considered "small," "medium," and "large" minimum size thresholds based on previous studies that have used medium-resolution satellite imagery to track supraglacial lake dynamics on the Greenland Ice Sheet (Table 1). The last category represents large supraglacial lakes. Since the swath width of SkySat (~9 km) is narrower than our 300 km^2 (~13 × 23 km) study site, single SkySat Collects do not cover our entire study site. We therefore aggregate our data to a monthly temporal resolution by computing the water fraction for each SkySat Collect and then averaging the water fractions for each month. Aggregating to monthly temporal resolution is a limitation since surface meltwater area can change rapidly but it is necessary for robustly documenting temporal changes over our study site using SkySat imagery.

4. Results

4.1. Performance of U-Net for Surface Meltwater Classification

We find that our U-Net classifies surface meltwater with an accuracy of 97% relative to our test data set (Table 2). The model's precision is higher than the recall, indicating that our classification contains few false positives but that there are some true positives that were not accurately detected. This is preferred because it means our classification provides a slightly conservative estimate of surface meltwater area. The U-Net performs accurately for all different types of SkySat product (i.e., "pansharpened," "analytic DN" and "analytic"; Table 2). This indicates that the U-Net is largely unaffected by radiometric correction and is able to accurately contextualize surface water in individual images regardless of processing level.

Our deep learning approach outperforms the global thresholding approach in terms of accuracy by five percentage points (Table 2). The accuracy of the global thresholding approach suffers from poor recall, in other words, failure to detect true positives. Recall could be improved by raising the value of the global threshold but that would come at a cost of reducing the precision. The global thresholding approach notably performs worse for non-radiometrically corrected images (i.e., "pansharpened"; Table 2), likely because this approach depends on consistent NDWI values across images. Given that SkySat acquires imagery from many different sensors, at

Table 1
Review of Studies That Have Developed Automated Approaches for Tracking Supraglacial Lakes Either Seasonally or Interannually on the Greenland Ice Sheet Using Satellite Remote Sensing

Study	Study site	Sensor	Approach	Minimum size threshold (m^2)
Glen et al. (2025)	West	S2, L8	Global threshold	1,800
Turton et al. (2021)	Northeast	S2	Global threshold	15,000
Hochreuther et al. (2021)	Northeast	S2	Global threshold	15,000
Fan et al. (2025)	All	S2	Global threshold	45,000
Miles et al. (2017)	West	S1, L8	Global threshold	49,500
Williamson et al. (2018)	West	S2, L8	Global threshold	49,500
Dunmire et al. (2025)	All	S1, S2, L8	Global threshold	50,000
Fitzpatrick et al. (2014)	West	MODIS	Global threshold	62,500
Rawlins et al. (2023)	North	S2	Global threshold	100,000
Liang et al. (2012)	West	MODIS	Adaptive threshold	125,000
Selmes et al. (2011)	All	MODIS	Global threshold	125,000
Morriss et al. (2013)	West	L7, MODIS	Global threshold	125,000
Hu et al. (2021)	All	S2	Random Forests	180,000
Cooley and Christoffersen (2017)	West	MODIS	Adaptive threshold	250,000

Note. This table is not meant to be exhaustive. Instead, it is meant to demonstrate the variety of approaches used by key studies that have advanced our understanding of surface meltwater dynamics.

different satellite elevation angles, and during different illumination conditions, the optimal NDWI threshold for classifying water likely varies substantially between images. We therefore caution against the use of global thresholds for classifying surface meltwater in SkySat imagery.

4.2. Dynamics of Surface Meltwater Ponding

Our automated U-Net mapping reveals that there are large variations in the area of surface water at our study site during the melt-season. Surface water covers 1.7% (or 5.0 km^2) of our study site in May, most of which is contained in small features (Figure 4). For example, water features <0.15 km^2 account for 92% of total surface water area and water features <0.015 km^2 account for 67.0%. Surface water area increases to 3.7% (or 11.3 km^2) of our study site between May and June in response to increasing meltwater runoff (Figure 4). The +6.3 km^2 increase in surface water area between May and June is driven by an increase (+7.3 km^2) in 12 large supraglacial lakes that offsets a decrease (−1.0 km^2) in smaller water features <0.15 km^2 (Figure 4). Maximum meltwater coverage at our study site is therefore caused by the filling of large supraglacial lakes.

4.3. Dynamics of Surface Meltwater Drainage

After maximum meltwater coverage in June, surface water area generally decreases throughout the rest of the summer (Figure 4). Our automated U-Net mapping demonstrates that surface water area decreases to 2.0%

Table 2
Performance of U-Net for Classifying Surface Meltwater From SkySat Imagery for Different Products

	All products			Pansharpened	Analytic DN	Analytic
	Acc	*Prec*	*Rec*	*Acc*	*Acc*	*Acc*
U-Net	0.97	0.97	0.85	0.96	0.98	0.97
Global thresholding	0.92	0.99	0.52	0.88	0.94	0.92

Note. The "pansharpened" products are not radiometrically corrected. "Analytic DN" products are radiometrically corrected but represent uncalibrated digital numbers. "Analytic" products are radiometrically corrected and transformed to top-of-atmosphere radiance. Also included for comparison is the performance of a more conventional global thresholding approach.

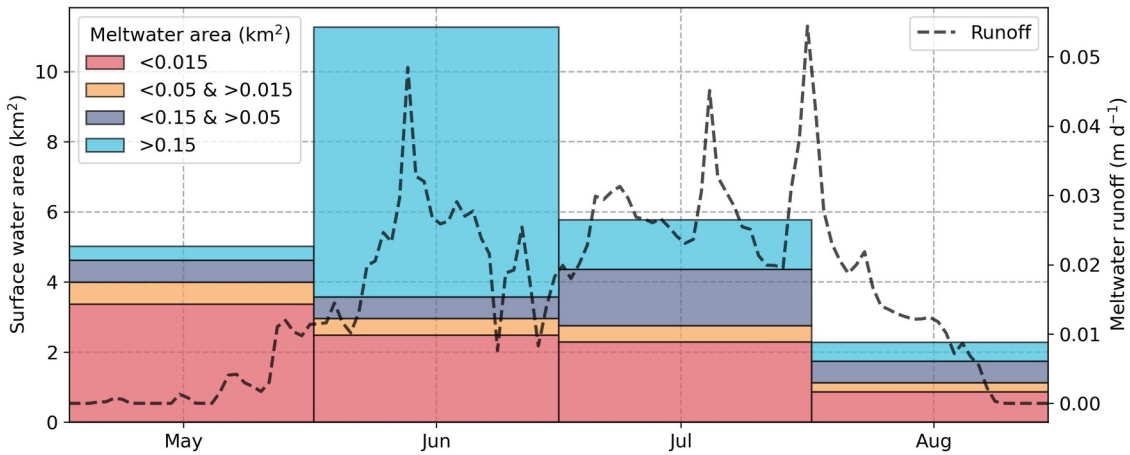

Figure 4. Seasonal variations of surface water area at our study site (~300 km^2) by size category. Surface water area rapidly increases between May and June due to the filling of large supraglacial lakes. Between June and July, these lakes begin to drain, causing a reduction in surface water area. Although most of the seasonality in surface water is caused by changes in large supraglacial lakes, a substantial amount of water is contained in smaller water features (<0.015 km^2), especially in May and August. Also shown is meltwater runoff at our study site from MAR v3.12 (Amory et al., 2021).

(6.0 km^2) in July. For comparison, Zhang et al. (2023) classified 1.5% of our study site as surface water between 29 July–5 August 2019. We attribute this difference to the high spatial resolution of SkySat imagery which is able to detect small water features (e.g., <0.015 km^2) more accurately than Sentinel-2 imagery. The decrease in surface water area is driven by reductions in large supraglacial lake areas which decrease by 6.3 km^2 between June and July (Figure 4). By August, surface water area decreases to 0.7% (2.3 km^2) of our study site: equivalent to an 80% loss of water area between maximum (June) and minimum (August) conditions.

With the exception on June, most water is contained in water features during our study period (Figure 4). Water features <0.15 km^2 account for 92.0% and 67.0% of total surface water area in May and August, respectively. However, water contained in smaller water features does not vary as much as large supraglacial lakes. The difference between maximum and minimum areas of small water features (<0.15 km^2) is ±2.9 km^2 at our study site (between May and August) whereas it is ±7.3 km^2 for the 12 large supraglacial lakes between May and June (Figure 4). The variation in very small water features (<0.015 km^2) is even less at ±2.5 km^2 (between May and August). Therefore, although smaller water features such as ponds and streams, account for the majority of surface water area during early- and late-summer, their areas fluctuate less than large supraglacial lakes.

4.4. Mechanisms of Supraglacial Lake Drainage

Our automated U-Net mapping reveals that several supraglacial lakes in our study site are connected by narrow supraglacial rivers (Lakes 1–7; Figure 5). We find that the formation of these rivers coincides with a cascading drainage event that causes a large reduction in supraglacial lake area in mid-June (Figure 4). Between 8–11 June, our individual lake analysis demonstrates that Lakes 6 and 7 partially drain, causing downstream lakes (Lakes 1, 2, 3, and 5) to fill (Figure 6). Then, between 11–13 June, Lake 5 partially drains, causing lakes downstream (Lake 1, 2, and 3) to continue filling. Finally, Lake 1 completely drains between 13–16 June causing all upstream lakes (Lake 2–7) to begin draining (Figure 7). Lake 1 loses 97% of its area between 13–16 June, thereby meeting the criteria for "rapid" drainage as defined by previous studies as a >80% reduction in lake area within a 2–6 day period (Figures 6 and 7) (Fitzpatrick et al., 2014; Morriss et al., 2013; Williamson et al., 2018). The six upstream lakes drain more slowly during the summer and become small lakes or supraglacial rivers by August (Figure 6). Therefore, the primary driver of supraglacial lake dynamics at our study site appears to be a cascading event that is facilitated by the development of hydrological connections between Lakes 1–7. We interpret these observations and discuss their implications in more detail in the Discussion section.

The other supraglacial lakes in our study site are isolated and our U-Net mapping demonstrates that there are no visible channels connecting them (Lakes 8–12). Three of these lakes are clustered in the NW of our study site and begin to drain between 13–16 June (Lake 11), 26 June–3 July (Lake 10), and 16–20 July (Lake 12) (Figure 8). The other two lakes nearer the center of our study site begin to drain between 13–16 June (Lake 8) and between 24–26

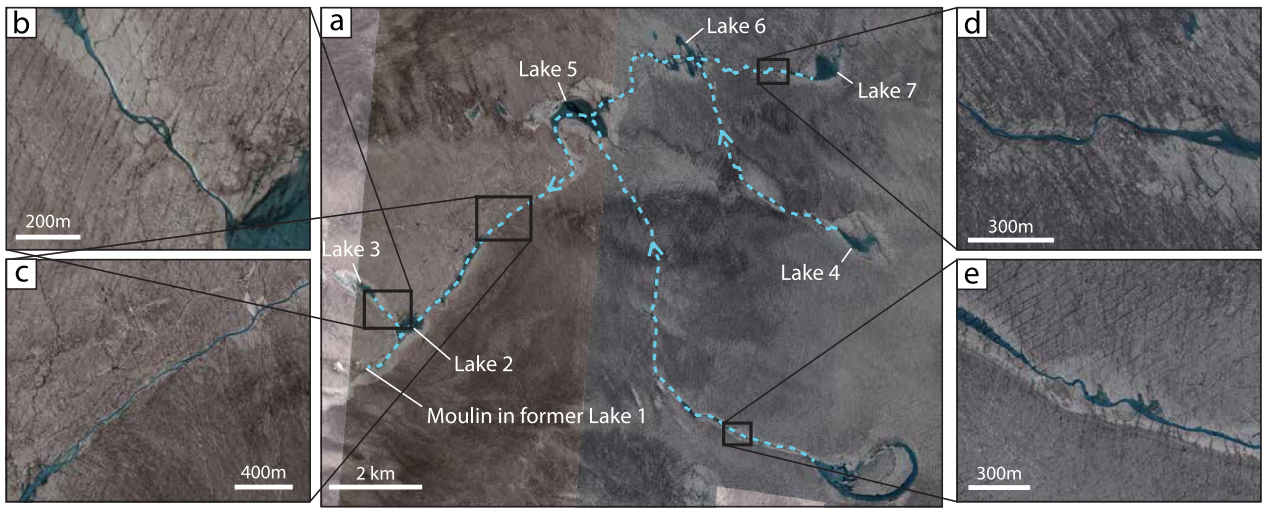

Figure 5. Supraglacial rivers between seven supraglacial lakes in our study site from high-resolution SkySat imagery. (a)–(e) These narrow supraglacial rivers, which form in mid-June, initiate a cascading drainage event that partially drains Lakes 6 and 7 between 8–11 June and Lake 5 between 11–13 June. These drainage events cause the downstream lakes (Lake 1–3) to fill rapidly such that when the Lake 1 subsequently drains, all upstream lakes (Lake 2–7) to begin draining. @ Planet Labs PBC 2025. All rights reserved.

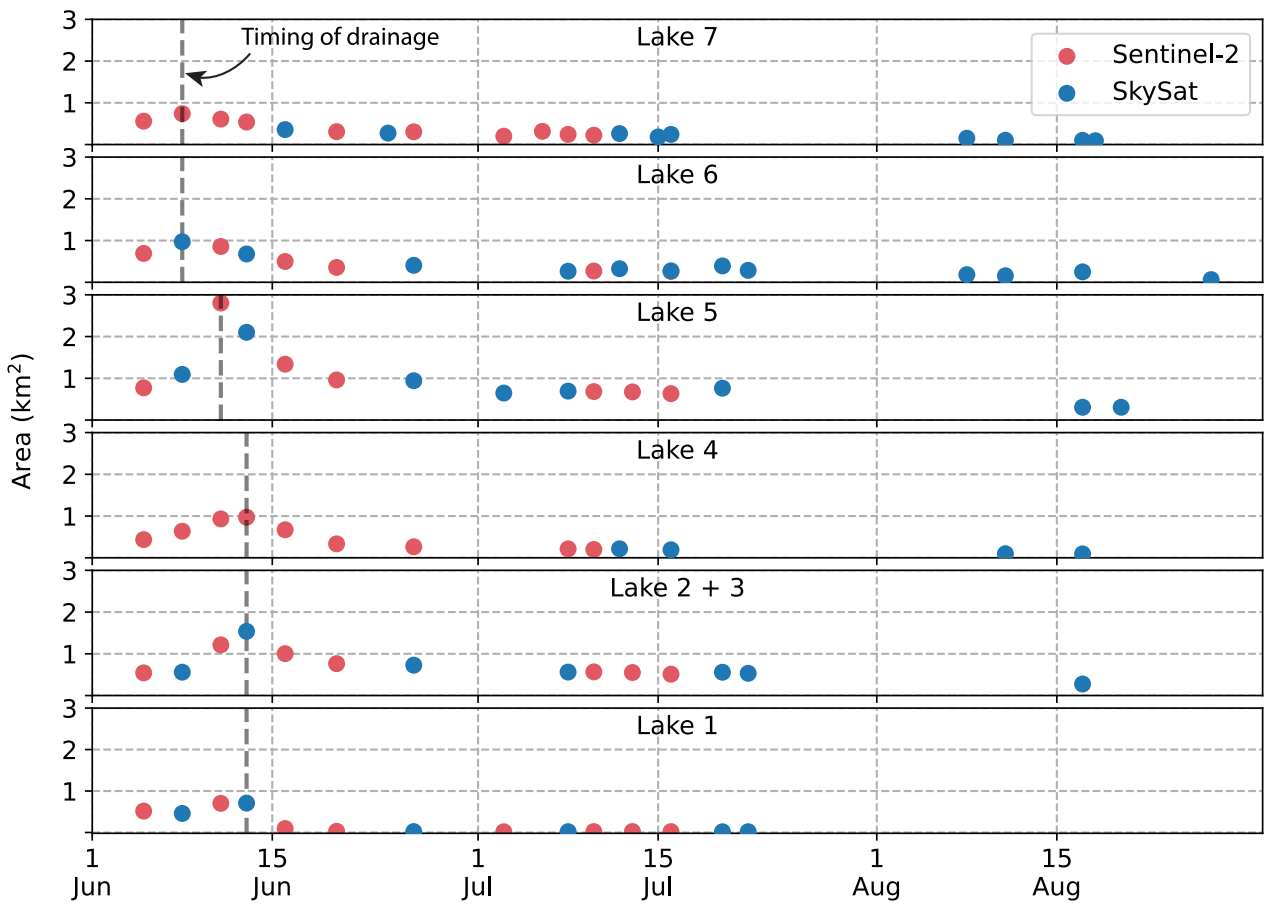

Figure 6. Timing of lake drainage for the linked network of lakes in our study site. Vertical dashed lines represent the earliest date that the lake begins to decrease in area. A cascading drainage event is initiated by the draining of Lakes 6 and 7 between 8–11 June, followed by the drainage of Lake 5 between 11–13 June. When the Lake 1 rapidly and completely drains, all upstream lakes (Lake 2–7) to begin draining.

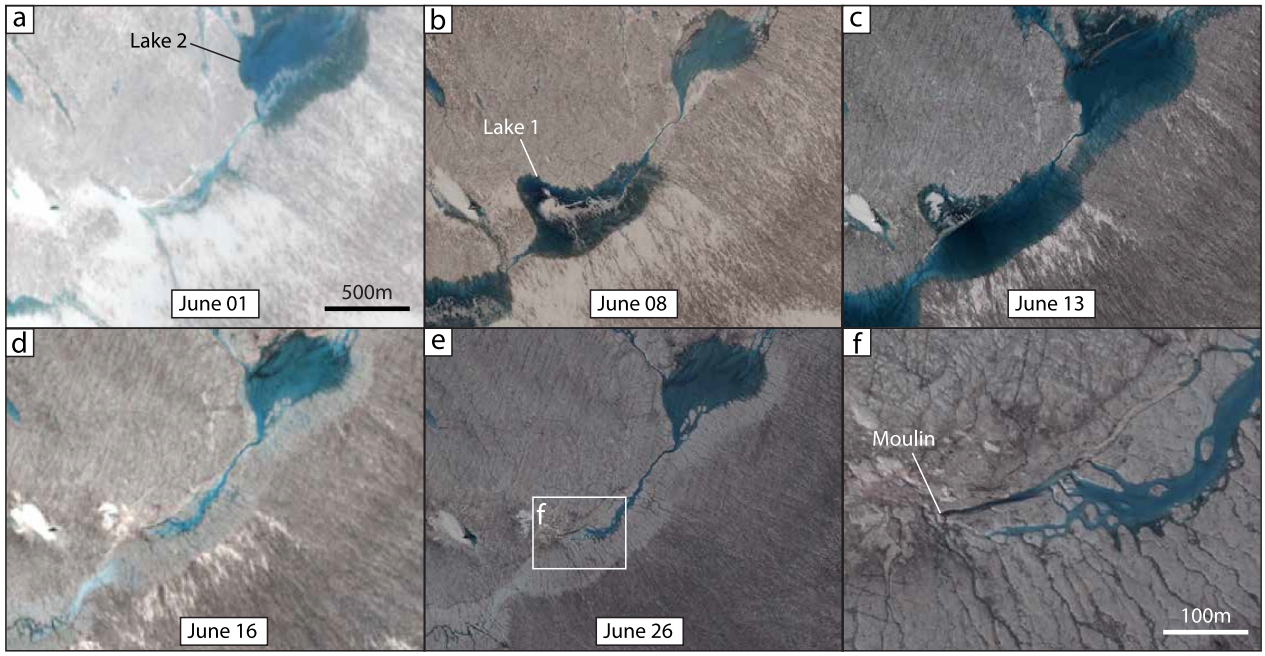

Figure 7. Sequence of events leading to the drainage of Lake 1 from SkySat (panels b, c, e, and f) and Sentinel-2 (panels a and d) imagery. Between 1–8 June and 8–13 June, Lake 1 fills because of the cascading drainage of upstream lakes. Between 13–16 June, Lake rapidly drains via a moulin that is clearly visible in SkySat imagery on 26 June. @ Planet Labs PBC 2025. All rights reserved.

June (Lake 9). The high-resolution SkySat imagery reveals that all the isolated lakes drain through moulins (Figure 9). In some cases (Lakes 9, 12), the moulin forms at the base of the lakebed (i.e., "bottom drainage"). In other cases (Lakes 8, 10, 11), an overspill channel forms that connects the lake to an existing moulin (i.e., "overspill drainage"; Figure 9). Lakes that drain at their lakebed exhibit more rapid area loss than those that drain via overspill. For example, our individual lake analysis demonstrates that Lake 12 loses ~90% of its area between 16–20 July and Lake 9 loses ~60% between 24–26 June (Figure 8). This indicates that "bottom drainage," as observed in Lakes 9 and 12, is more likely to be associated with rapid drainage events, a finding that corroborates Tedesco et al. (2013). Overall, the variety of lake drainage timings, rates, and mechanisms that we observe at our study site provides insight into supraglacial lake dynamics that are discussed in the next section.

5. Discussion

5.1. Dynamics of Surface Meltwater Ponding and Drainage

We applied deep learning to SkySat imagery to investigate surface water dynamics within a ~300 km^2 study site in the western Greenland Ice Sheet ablation zone. Despite the relatively limited spatial coverage, the high spatial resolution of the imagery provided by the SkySat constellation during the summer of 2019 provides several insights into the surface hydrology in this sector of the ice sheet. We find that, during the early-summer (June), most (71%) of the surface water (by area) is contained in 12 large supraglacial lakes. Likewise, most of the seasonality in surface water area, which attains a maximum in June and minimum in August, can be attributed to a reduction in supraglacial lake area (Figure 4). Our findings therefore confirm that medium-resolution imagery (i.e. Sentinel-2, Landsat 8) can be used to track changes for the majority of surface water across the western ice sheet ablation zone. Having said that, a substantial portion of the total surface meltwater is contained in small features, particularly at the beginning and end of the summer. We demonstrate that 67% and 38% of surface water is found in small water features (<0.015 km^2) in May and August, respectively (Figure 4). Studies which apply minimum size thresholds when mapping surface water using medium-resolution satellite imagery (Table 1) therefore likely *underestimate* the total surface water area and *overestimate* the seasonality in surface water area. Consequently, they may also underestimate the radiative effect caused by meltwater ponding (Ryan et al., 2025).

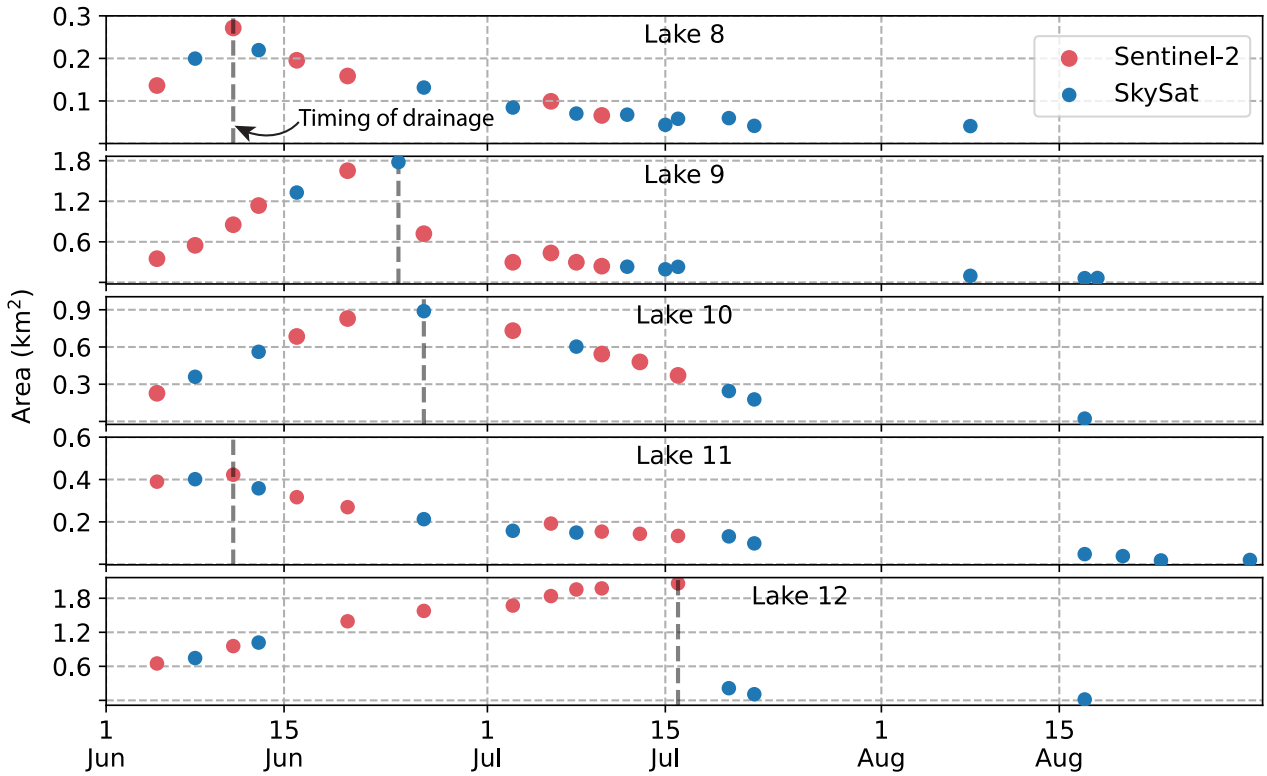

Figure 8. Timing of lake drainage for the isolated lakes in our study site. All lakes drain at different times during the summer and lakes that experience "bottom drainage" (Lakes 9 and 12) drain more rapidly that lakes that overspill (Lakes 8, 10, and 11).

5.2. Supraglacial Lake Drainage Mechanisms Revealed by High-Resolution Imagery

Our study demonstrates that supraglacial lake drainage mechanisms can be reliably identified using high spatial resolution (i.e. ~1 m) SkySat imagery. We find that some of the lakes at our study site drain because a moulin forms at the base of the lake while others drain because they overspill into a nearby moulin (Figure 9). Both these drainage mechanisms have been previously documented by field studies (Doyle et al., 2013; Stevens et al., 2015; Tedesco et al., 2013). Most lakes in our study site, however, drain via a mechanism that has not been documented by either field studies or remote sensing. During early-summer, the high-resolution imagery reveals that the formation of supraglacial rivers between lakes initiates a cascading drainage event that causes the most downstream lakes to rapidly fill (i.e., Lake 1–3; Figure 6). When Lake 1 subsequently drains, the upstream lakes (i.e., Lakes 2–7) begin to drain as well because they are hydrologically connected (Figure 5). This mechanism of lake drainage, which we term "linked drainage," therefore appears to be remotely triggered by overspilling of lakes upstream, as opposed to locally triggered at a downstream lakebed. Future tasking of the SkySat constellation (or other satellite platforms with similar resolution) could be used to investigate whether this type of drainage mechanism repeats in other years or is common in other sectors of ice sheet.

The "linked" drainage mechanism that we identify may explain several puzzling observations of supraglacial lake drainage that have been challenging to interpret using medium-resolution satellite imagery (Poinar & Andrews, 2021). For example, several studies have observed drainage of supraglacial lakes in ice flow regimes that are thought to be too compressive for hydrofracture (Christoffersen et al., 2018; Poinar & Andrews, 2021; Stevens et al., 2015). It is generally assumed that local stress perturbations which temporarily overcome background compressive stresses are required for hydrofracture and lake drainage (e.g., Stevens et al., 2015). Our observations indicate that such precursory events are not necessarily required. Instead, we demonstrate that lake drainage in compressive regimes can be explained by the formation of hydrological connections (i.e., narrow streams) with downstream lakes situated in more extensional ice flow regimes. The subsequent drainage of the downstream lake (i.e. Lake 1) causes all lakes to drain regardless of which flow regime they are situated in. This "linked" drainage mechanism therefore provides a plausible explanation for the drainage of supraglacial lakes

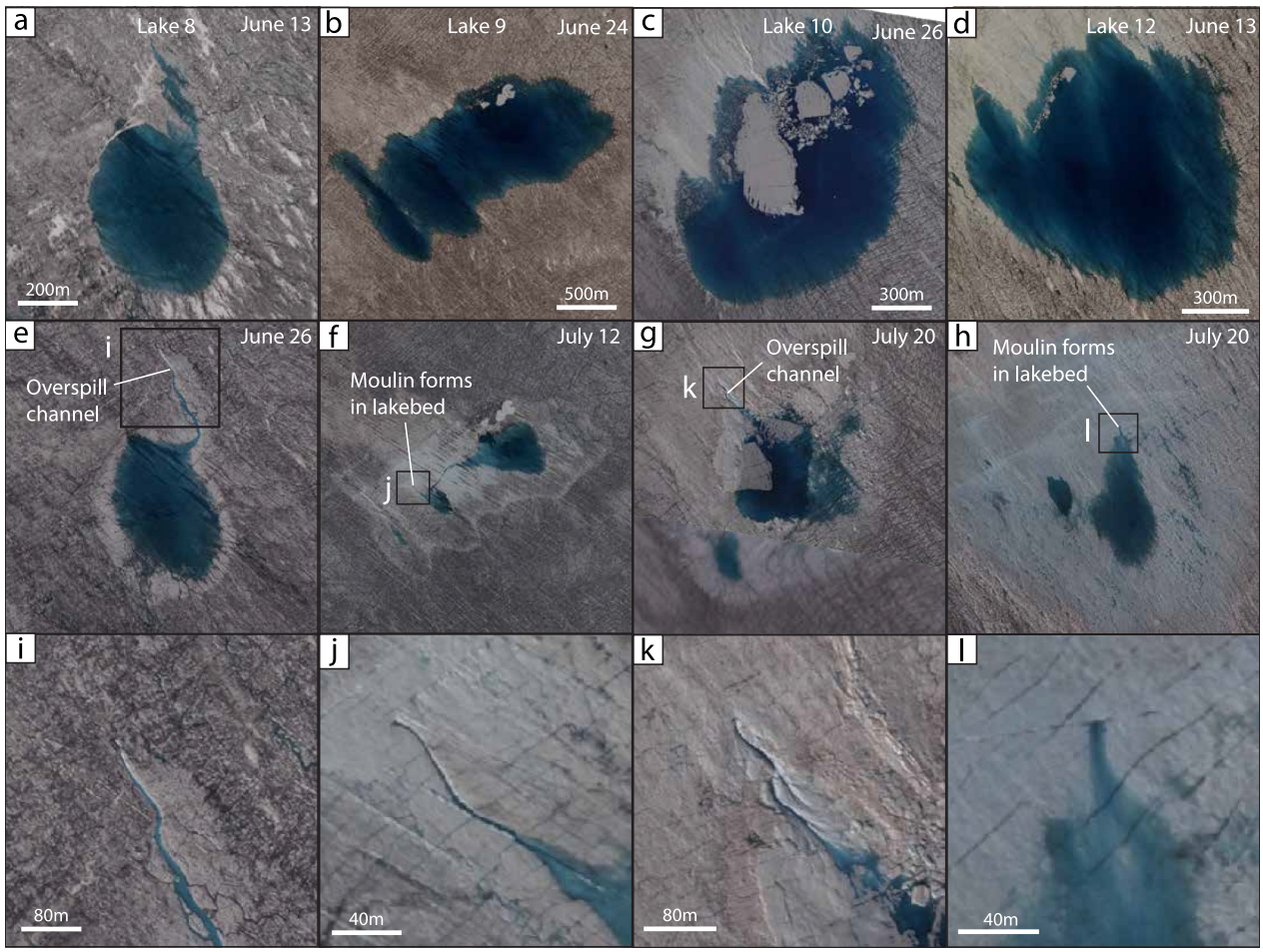

Figure 9. Drainage mechanisms of isolated lakes in our study site from high-resolution SkySat imagery. (a)–(d) Lakes immediately prior to drainage. (e)–(h) Lakes after drainage. (i)–(l) Zoom to moulin. Some lakes connect to moulins via overspill channels (Lake 8 and 10) while others drain into moulins formed at the base of the lake (Lake 9 and 12). @ Planet Labs PBC 2025. All rights reserved.

located in compressive ice flow regimes and may be at least partly responsible for the lack of significant correlations between lake drainages and ice flow regimes noted by previous studies (Poinar & Andrews, 2021; Williamson et al., 2018).

Likewise, several studies have documented synchronous or "cascading" supraglacial lake drainage where multiple lakes, often tens of kilometers apart, drain at the same time (Doyle et al., 2013; Fitzpatrick et al., 2014; Maier et al., 2023). These studies have attributed such patterns to "tensile shock" whereby one lake drainage causes transient uplift and longitudinal strain that perturbs the stress fields near other lakes, triggering further hydrofracturing (Christoffersen et al., 2018; Hoffman et al., 2018). However, our findings indicate that this mechanism is not necessarily required for synchronous lake drainage. By resolving narrow, incised supraglacial rivers that are often <5 m wide with SkySat imagery, we demonstrate that lake drainage synchronicity at our study site can be attributed to hydrological connectivity between supraglacial lakes. Our findings therefore indicate that not all synchronous lake drainages should be attributed to "tensile shock" (e.g., Christoffersen et al., 2018; Hoffman et al., 2018). We note that this conclusion corroborates Stevens et al. (2024) who showed that the length-scale of elastic stress-coupling is unlikely to be more than a few kilometers. We therefore recommend that studies use high-resolution imagery, where available, to investigate the presence or absence of connecting channels before invoking stress-coupling and hydrofracture to explain synchronous lake drainages.

We interpret the drainage of Lake 1 as evidence for full-depth hydrofracture, given its rate and completeness (97% in <3 days; Figure 7). The causes of hydrofracture, however, are unclear. It is possible that hydrofracture was triggered by a precursory event (e.g., basal slip) that perturbed local ice stresses near the lake (e.g., Stevens

et al., 2015). On the other hand, it is possible that hydrofracture was triggered once the lake attained a specific volume (e.g., Chudley et al., 2019). If this was the case, then precursory stress perturbations may not be required to trigger synchronous drainage of supraglacial lakes. Higher temporal resolution ice flow data, such as that acquired by in situ GPS, would be required to investigate causes of hydrofracture at Lake 1.

Before hydrofracture is initiated, supraglacial lakes in our study site rapidly fill in early-June (Figures 6 and 8). This indicates that there is a lack of surface-to-bed connections (i.e., moulins) during the early-summer either because moulins have not yet formed or because they are situated outside the lake basin. This causes the rapid filling of supraglacial lakes that may explain differences in proglacial river outflow and meltwater runoff during early-summer. For example, discharge from the Isortoq River, a proglacial river draining Isunguata Sermia in western Greenland, was initially insensitive to substantial increases in meltwater runoff in June 2012 (Smith et al., 2015). Likewise, discharge from the Leverett Glacier outlet, a proglacial river 16 km south of the Isortoq River, lags increases in meltwater runoff in early June 2012 (Mankoff et al., 2020). The difference between modeled meltwater runoff and proglacial discharge during the early-summer is likely explained by temporary storage of water in the supra- or sub-glacial system (Rennermalm et al., 2013). While our findings cannot partition these two sources of water storage, we can confirm that early-season ponding of meltwater on the surface of the ice sheet contributes to temporal mismatches between proglacial runoff and meltwater production.

5.3. Unlocking the Potential of Satellite Constellations With Deep Learning

In this study, we used imagery from the SkySat constellation to map surface water on the Greenland Ice Sheet. Although SkySat satellites have much narrower swath width than medium-resolution satellite platforms such as Sentinel-2, they provide imagery with similar revisit times because the SkySat constellation consisted of 13 satellites in sun-synchronous orbits during the summer of 2019. There are currently 15 SkySat satellites in sun-synchronous, suggesting that future tasking could achieve even greater revisit frequency and spatial coverage. The advantage of SkySat is that it provides 10× higher spatial resolution imagery than Sentinel-2, which makes small features such as moulins and supraglacial channels easier to identify (e.g., Figure 7d vs. Figure 7e). In fact, imagery from the SkySat constellation is closer to that collected by fixed-wing drones (e.g., Jones et al., 2018; Jouvet et al., 2019; Ryan et al., 2018) than to other satellite sensors. But while logistical challenges usually limit the temporal coverage of drone imagery to a few days or weeks, a tasked SkySat constellation could potentially collect regular imagery over a study site that is hundreds of square kilometers in area, year-round. SkySat imagery therefore fills a technological niche that provides higher spatial resolution than Sentinel-2 and Landsat and better temporal continuity than drone imagery. We note that the SkySat imagery used by our study is a subset of the imagery collected by a tasking campaign conducted during the summer of 2019. This larger collection of SkySat imagery could be used to investigate the transferability of our approach and findings to other regions of the ice sheet. Likewise, future tasking of SkySat over tidewater glaciers or ice shelves could provide valuable insight into other key glaciological processes.

The challenge with SkySat imagery is that it is acquired by different sensors, at different times of the day, and at different satellite elevation angles. Conventional thresholding approaches developed for mapping surface water in medium-resolution imagery therefore cannot be justified since the optimal threshold for differentiating water from ice and snow likely changes from image-to-image. In response to this challenge, we developed a task-specific CN based on the U-Net architecture to classify surface water on the Greenland Ice Sheet. The advantage of a CN is that it can learn spatial features (e.g., edges, textures, or shapes) in the data by performing successive image transformations (i.e., convolutions) on different spatial scales (i.e., pooling). CNs can therefore identify both low-level and high-level features that describe surface water in SkySat imagery, leading to accuracies of 97% (precision: 97% and recall: 85%) (Table 2). The accuracy we achieved is comparable to the only other study (accuracy: 99%, precision: 90% and recall: 91%) that used a U-Net to classify surface meltwater in Northeast Greenland using Sentinel-2 imagery (Lutz et al., 2023). It is also five percentage points higher than a more conventional approach for mapping surface water (i.e., global thresholding). Given the accuracy for mapping surface water on ice sheets, we anticipate that the use of CNs will become more common in cryospheric remote sensing, especially given their potential for automatically classifying the growing number of high-resolution image collections acquired by satellite constellations.

We suggest that the accuracy and spatial resolution of our surface water maps mean they could be used as ground-truth for studies investigating surface water dynamics on the Greenland Ice Sheet using other sensors. Many of

these studies classify supraglacial lakes and ponds by applying global thresholds to either individual bands or band indices (Table 1). While a global thresholding approach may be justified for mapping large supraglacial lakes, it is likely not appropriate for mapping small, shallow features such as ponds because the optimal threshold for distinguishing surface meltwater varies regionally and seasonally due to changing illumination conditions. To avoid misclassifications, studies commonly introduce size thresholds to remove small, isolated pixels classified as water (Table 1). Yet few studies evaluate the impact that this decision has on their reported findings. Our high-resolution surface water maps could be used to characterize expected biases from different minimum size thresholds. Likewise, our maps could be used to understand the effects of mixed-pixels on surface water classification. Our findings may therefore provide a benchmark for evaluating uncertainties in surface water maps derived from medium-to coarse-resolution satellite imagery.

6. Conclusions

We investigated surface water dynamics within a 300 km^2 study site in the western Greenland Ice Sheet ablation zone by applying deep learning to imagery collected by the SkySat constellation. We found that our deep learning approach robustly classified surface water with accuracies of 97% despite imagery being collected by many different sensors, at different satellite elevation angles, and with different illumination conditions. Furthermore, we found that our approach was five percentage points more accurate than a global thresholding approach, which is currently the most common method for classifying water in medium-resolution imagery (Table 2). Our findings corroborate a previous study which found that CNs provide more accurate semantic segmentation of surface water than conventional global thresholding approaches over ice sheets (Lutz et al., 2023). Deep learning therefore improves our ability to extract valuable information from vast quantities of imagery collected by satellite constellations for observing ice sheet processes.

By accurately mapping surface water in high-resolution SkySat imagery, we were able to investigate the dynamics of water features ranging from small ponds and streams to large supraglacial lakes. We found that although most surface water is contained in 12 large supraglacial lakes, small water features (<0.015 km^2) contribute to a substantial fraction of total surface water (67% in May to 38% in August). Studies that use minimum size thresholds therefore likely underestimate the total surface water area and overestimate seasonal changes in surface water area, with implications for quantifying the radiative effect caused by meltwater ponding. Likewise, the high-resolution imagery allowed us to accurately characterize mechanisms of supraglacial lake drainage that have traditionally only been provided by field measurements. By resolving narrow channels that connect several supraglacial lakes in our study region, we describe a "linked" drainage mechanism that explains the near-synchronous drainage of seven supraglacial lakes in mid-June. This previously overlooked mechanism demonstrates that, when lakes become hydrologically connected, the drainage of a downstream lake can trigger widespread, synchronous lake drainages over distances greater than 10 km. The linked mechanism that we identified may explain why (a) supraglacial lake drainage can occur in compressive ice flow regimes, provided that lakes are hydrologically connected to a moulin located in an extensional flow regime and (b) synchronous or "cascading" lake drainages can occur without invoking elastic stress-coupling or "tensile shock." While our observations are limited to a relatively small study site, our findings provide plausible explanations for several ambiguous, and seemingly contradictory, observations of supraglacial lake drainage patterns in other areas of the ice sheet. We recommend that future studies consider the possibility of linked drainage when investigating coupling between supraglacial lake drainage and ice dynamics at regional or ice-sheet scales.

Conflict of Interest

The authors declare no conflicts of interest relevant to this study.

Data Availability Statement

The code is available at: https://doi.org/10.5281/zenodo.17651099 (Ryan, 2025a).

The data is available at: https://doi.org/10.5281/zenodo.17650985 (Ryan, 2025b).

Acknowledgments
This work used data made available through the NASA Commercial SmallSat Data Acquisition (CSDA) Program. This research was supported by NASA award 80NSSC25K0325. We thank Izaiah Williams for assistance with downloading SkySat imagery. We thank Xavier Fettweis for making the MARv3.12 outputs available.

References

Alley, R. B., Dupont, T. K., Parizek, B. R., & Anandakrishnan, S. (2005). Access of surface meltwater to beds of sub-freezing glaciers: Preliminary insights. *Annals of Glaciology*, *40*, 8–14. https://doi.org/10.3189/172756405781813483

Amory, C., Kittel, C., Le Toumelin, L., Agosta, C., Delhasse, A., Favier, V., & Fettweis, X. (2021). Performance of MAR (v3.11) in simulating the drifting-snow climate and surface mass balance of Adélie Land, East Antarctica. *Geoscientific Model Development*, *14*(6), 3487–3510. https://doi.org/10.5194/gmd-14-3487-2021

Bhushan, S., Shean, D., Alexandrov, O., & Henderson, S. (2021). Automated digital elevation model (DEM) generation from very-high-resolution Planet SkySat triplet stereo and video imagery. *ISPRS Journal of Photogrammetry and Remote Sensing*, *173*, 151–165. https://doi.org/10.1016/j.isprsjprs.2020.12.012

Chandler, D. M., & Hubbard, A. (2023). Widespread partial-depth hydrofractures in ice sheets driven by supraglacial streams. *Nature Geoscience*, *16*(7), 605–611. https://doi.org/10.1038/s41561-023-01208-0

Christoffersen, P., Bougamont, M., Hubbard, A., Doyle, S. H., Grigsby, S., & Pettersson, R. (2018). Cascading lake drainage on the Greenland Ice Sheet triggered by tensile shock and fracture. *Nature Communications*, *9*(1), 1064. https://doi.org/10.1038/s41467-018-03420-8

Chudley, T. R., Christoffersen, P., Doyle, S. H., Bougamont, M., Schoonman, C. M., Hubbard, B., & James, M. R. (2019). Supraglacial lake drainage at a fast-flowing Greenlandic outlet glacier. *Proceedings of the National Academy of Sciences*, *116*(51), 25468–25477. https://doi.org/10.1073/pnas.1913685116

Chudley, T. R., Christoffersen, P., Doyle, S. H., Dowling, T. P. F., Law, R., Schoonman, C. M., et al. (2021). Controls on water storage and drainage in crevasses on the Greenland Ice Sheet. *Journal of Geophysical Research: Earth Surface*, *126*(9), e2021JF006287. https://doi.org/10.1029/2021JF006287

Cooley, S. W., & Christoffersen, P. (2017). Observation bias correction reveals more rapidly draining lakes on the Greenland Ice Sheet. *Journal of Geophysical Research: Earth Surface*, *122*(10), 1867–1881. https://doi.org/10.1002/2017JF004255

Das, S. B., Joughin, I., Behn, M. D., Howat, I. M., King, M. A., Lizarralde, D., & Bhatia, M. P. (2008). Fracture propagation to the base of the Greenland Ice Sheet during supraglacial Lake drainage. *Science*, *320*(5877), 778–781. https://doi.org/10.1126/science.1153360

Datta, R. T., & Wouters, B. (2021). Supraglacial lake bathymetry automatically derived from ICESat-2 constraining lake depth estimates from multi-source satellite imagery. *The Cryosphere*, *15*(11), 5115–5132. https://doi.org/10.5194/tc-15-5115-2021

Doyle, S. H., Hubbard, A. L., Dow, C. F., Jones, G. A., Fitzpatrick, A., Gusmeroli, A., et al. (2013). Ice tectonic deformation during the rapid in situ drainage of a supraglacial lake on the Greenland Ice Sheet. *The Cryosphere*, *7*(1), 129–140. https://doi.org/10.5194/tc-7-129-2013

Dunmire, D., Subramanian, A. C., Hossain, E., Gani, M. O., Banwell, A. F., Younas, H., & Myers, B. (2025). Greenland ice sheet wide supraglacial Lake evolution and dynamics: Insights from the 2018 and 2019 melt seasons. *Earth and Space Science*, *12*(2), e2024EA003793. https://doi.org/10.1029/2024EA003793

Fan, Y., Ke, C.-Q., Luo, L., Shen, X., Livingstone, S. J., & Lea, J. M. (2025). Expansion of supraglacial lake area, volume and extent on the Greenland ice sheet from 1985 to 2023. *Journal of Glaciology*, *71*, e4. https://doi.org/10.1017/jog.2024.87

Fitzpatrick, A. A. W., Hubbard, A. L., Box, J. E., Quincey, D. J., Van As, D., Mikkelsen, A. P. B., et al. (2014). A decade (2002–2012) of supraglacial lake volume estimates across Russell Glacier, West Greenland. *The Cryosphere*, *8*(1), 107–121. https://doi.org/10.5194/tc-8-107-2014

Glen, E., Leeson, A., Banwell, A. F., Maddalena, J., Corr, D., Atkins, O., et al. (2025). A comparison of supraglacial meltwater features throughout contrasting melt seasons: Southwest Greenland. *The Cryosphere*, *19*(3), 1047–1066. https://doi.org/10.5194/tc-19-1047-2025

Hochreuther, P., Neckel, N., Reimann, N., Humbert, A., & Braun, M. (2021). Fully automated detection of supraglacial Lake Area for Northeast Greenland using Sentinel-2 time-series. *Remote Sensing*, *13*(2), 205. https://doi.org/10.3390/rs13020205

Hoffman, M. J., Perego, M., Andrews, L. C., Price, S. F., Neumann, T. A., Johnson, J. V., et al. (2018). Widespread moulin formation during supraglacial Lake drainages in Greenland. *Geophysical Research Letters*, *45*(2), 778–788. https://doi.org/10.1002/2017GL075659

Hu, J., Huang, H., Chi, Z., Cheng, X., Wei, Z., Chen, P., et al. (2021). Distribution and evolution of supraglacial Lakes in Greenland during the 2016–2018 melt seasons. *Remote Sensing*, *14*(1), 55. https://doi.org/10.3390/rs14010055

Jacobsen, K. (2022). Mapping with SkySat images. In *The international archives of the photogrammetry, remote sensing and spatial information sciences, XLIII-B1-2022* (pp. 99–106). https://doi.org/10.5194/isprs-archives-XLIII-B1-2022-99-2022

Jones, C., Ryan, J., Holt, T., & Hubbard, A. (2018). Structural glaciology of Isunguata Sermia, West Greenland. *Journal of Maps*, *14*(2), 517–527. https://doi.org/10.1080/17445647.2018.1507952

Jouvet, G., Weidmann, Y., Van Dongen, E., Lüthi, M. P., Vieli, A., & Ryan, J. C. (2019). High-Endurance UAV for monitoring calving glaciers: Application to the inglefield Bredning and Eqip Sermia, Greenland. *Frontiers in Earth Science*, *7*, 206. https://doi.org/10.3389/feart.2019.00206

Kingma, D. P., & Ba, J. (2017). Adam: A method for stochastic optimization (no. arXiv:1412.6980). *arXiv*. https://doi.org/10.48550/arXiv.1412.6980

Kingslake, J., Ng, F., & Sole, A. (2015). Modelling channelized surface drainage of supraglacial lakes. *Journal of Glaciology*, *61*(225), 185–199. https://doi.org/10.3189/2015JoG14J158

Liang, Y.-L., Colgan, W., Lv, Q., Steffen, K., Abdalati, W., Stroeve, J., et al. (2012). A decadal investigation of supraglacial lakes in West Greenland using a fully automatic detection and tracking algorithm. *Remote Sensing of Environment*, *123*, 127–138. https://doi.org/10.1016/j.rse.2012.03.020

Lüthje, M., Pedersen, L. T., Reeh, N., & Greuell, W. (2006). Modelling the evolution of supraglacial lakes on the West Greenland ice-sheet margin. *Journal of Glaciology*, *52*(179), 608–618. https://doi.org/10.3189/172756506781828386

Lutz, K., Bahrami, Z., & Braun, M. (2023). Supraglacial lake evolution over Northeast Greenland using deep learning methods. *Remote Sensing*, *15*(17), 4360. https://doi.org/10.3390/rs15174360

Macdonald, G. J., Banwell, A. F., & MacAyeal, D. R. (2018). Seasonal evolution of supraglacial lakes on a floating ice tongue, Petermann Glacier, Greenland. *Annals of Glaciology*, *59*(76pt1), 56–65. https://doi.org/10.1017/aog.2018.9

Maier, N., Andersen, J. K., Mouginot, J., Gimbert, F., & Gagliardini, O. (2023). Wintertime supraglacial lake drainage Cascade triggers large-scale ice flow response in Greenland. *Geophysical Research Letters*, *50*(4), e2022GL102251. https://doi.org/10.1029/2022GL102251

Mankoff, K. D., Noël, B., Fettweis, X., Ahlstrøm, A. P., Colgan, W., Kondo, K., et al. (2020). Greenland liquid water discharge from 1958 through 2019. *Earth System Science Data*, *12*(4), 2811–2841. https://doi.org/10.5194/essd-12-2811-2020

Miles, K. E., Willis, I. C., Benedek, C. L., Williamson, A. G., & Tedesco, M. (2017). Toward monitoring surface and subsurface lakes on the Greenland Ice Sheet using Sentinel-1 SAR and Landsat-8 OLI imagery. *Frontiers in Earth Science*, *5*, 58. https://doi.org/10.3389/feart.2017.00058

Morriss, B. F., Hawley, R. L., Chipman, J. W., Andrews, L. C., Catania, G. A., Hoffman, M. J., et al. (2013). A ten-year record of supraglacial lake evolution and rapid drainage in West Greenland using an automated processing algorithm for multispectral imagery. *The Cryosphere*, *7*(6), 1869–1877. https://doi.org/10.5194/tc-7-1869-2013

Poinar, K., & Andrews, L. C. (2021). Challenges in predicting Greenland supraglacial lake drainages at the regional scale. *The Cryosphere*, *15*(3), 1455–1483. https://doi.org/10.5194/tc-15-1455-2021

Rawlins, L. D., Rippin, D. M., Sole, A. J., Livingstone, S. J., & Yang, K. (2023). Seasonal evolution of the supraglacial drainage network at Humboldt Glacier, northern Greenland, between 2016 and 2020. *The Cryosphere*, *17*(11), 4729–4750. https://doi.org/10.5194/tc-17-4729-2023

Rennermalm, A. K., Smith, L. C., Chu, V. W., Box, J. E., Forster, R. R., Van Den Broeke, M. R., et al. (2013). Evidence of meltwater retention within the Greenland Ice Sheet. *The Cryosphere*, *7*(5), 1433–1445. https://doi.org/10.5194/tc-7-1433-2013

Ronneberger, O., Fischer, P., & Brox, T. (2015). U-Net: Convolutional networks for biomedical image segmentation (no. arXiv:1505.04597). *arXiv*. https://doi.org/10.48550/arXiv.1505.04597

Ryan, J. C. (2025a). JohnnyRyan1/skysat: November 19, 2025 release (version 2) [Software]. *Zenodo*. https://doi.org/10.5281/zenodo.17651099

Ryan, J. C. (2025b). Data for "Mechanisms of surface meltwater ponding and drainage on the Greenland Ice Sheet revealed using SkySat imagery and deep learning" (Version 1) [Dataset]. *Zenodo*. https://doi.org/10.5281/zenodo.17650985

Ryan, J. C., Cooper, M. G., Cooley, S. W., Rennermalm, Å. K., & Smith, L. C. (2025). Meltwater ponding has an underestimated radiative effect on the surface of the Greenland Ice Sheet. *Nature Communications*, *16*(1), 8274. https://doi.org/10.1038/s41467-025-62503-5

Ryan, J. C., Hubbard, A., Stibal, M., Irvine-Fynn, T. D., Cook, J., Smith, L. C., et al. (2018). Dark zone of the Greenland Ice Sheet controlled by distributed biologically-active impurities. *Nature Communications*, *9*(1), 1065. https://doi.org/10.1038/s41467-018-03353-2

Schoof, C. (2010). Ice-sheet acceleration driven by melt supply variability. *Nature*, *468*(7325), 803–806. https://doi.org/10.1038/nature09618

Selmes, N., Murray, T., & James, T. D. (2011). Fast draining lakes on the Greenland Ice Sheet. *Geophysical Research Letters*, *38*(15), 2011GL047872. https://doi.org/10.1029/2011GL047872

Shen, C. (2018). A transdisciplinary review of deep learning research and its relevance for water resources scientists. *Water Resources Research*, *54*(11), 8558–8593. https://doi.org/10.1029/2018WR022643

Smith, L. C., Chu, V. W., Yang, K., Gleason, C. J., Pitcher, L. H., Rennermalm, A. K., et al. (2015). Efficient meltwater drainage through supraglacial streams and rivers on the southwest Greenland ice sheet. *Proceedings of the National Academy of Sciences*, *112*(4), 1001–1006. https://doi.org/10.1073/pnas.1413024112

Smith, L. C., Yang, K., Pitcher, L. H., Overstreet, B. T., Chu, V. W., Rennermalm, Å. K., et al. (2017). Direct measurements of meltwater runoff on the Greenland ice sheet surface. *Proceedings of the National Academy of Sciences*, *114*(50), E10622–E10631. https://doi.org/10.1073/pnas.1707743114

Stevens, L. A., Behn, M. D., Das, S. B., Joughin, I., Noël, B. P. Y., Van Den Broeke, M. R., & Herring, T. (2016). Greenland Ice Sheet flow response to runoff variability. *Geophysical Research Letters*, *43*(21), 11295–11303. https://doi.org/10.1002/2016GL070414

Stevens, L. A., Behn, M. D., McGuire, J. J., Das, S. B., Joughin, I., Herring, T., et al. (2015). Greenland supraglacial lake drainages triggered by hydrologically induced basal slip. *Nature*, *522*(7554), 73–76. https://doi.org/10.1038/nature14480

Stevens, L. A., Das, S. B., Behn, M. D., McGuire, J. J., Lai, C., Joughin, I., et al. (2024). Elastic stress coupling between supraglacial Lakes. *Journal of Geophysical Research: Earth Surface*, *129*(5), e2023JF007481. https://doi.org/10.1029/2023JF007481

Tedesco, M., Lüthje, M., Steffen, K., Steiner, N., Fettweis, X., Willis, I., et al. (2012). Measurement and modeling of ablation of the bottom of supraglacial lakes in western Greenland. *Geophysical Research Letters*, *39*(2), 2011GL049882. https://doi.org/10.1029/2011GL049882

Tedesco, M., Willis, I. C., Hoffman, M. J., Banwell, A. F., Alexander, P., & Arnold, N. S. (2013). Ice dynamic response to two modes of surface lake drainage on the Greenland ice sheet. *Environmental Research Letters*, *8*(3), 034007. https://doi.org/10.1088/1748-9326/8/3/034007

Turton, J. V., Hochreuther, P., Reimann, N., & Blau, M. T. (2021). The distribution and evolution of supraglacial lakes on 79° N Glacier (northeastern Greenland) and interannual climatic controls. *The Cryosphere*, *15*(8), 3877–3896. https://doi.org/10.5194/tc-15-3877-2021

Van De Wal, R. S. W., Boot, W., Van Den Broeke, M. R., Smeets, C. J. P. P., Reijmer, C. H., Donker, J. J. A., & Oerlemans, J. (2008). Large and rapid melt-induced velocity changes in the ablation zone of the Greenland ice sheet. *Science*, *321*(5885), 111–113. https://doi.org/10.1126/science.1158540

Wang, Y., & Sugiyama, S. (2024). Supraglacial lake evolution on Tracy and Heilprin Glaciers in northwestern Greenland from 2014 to 2021. *Remote Sensing of Environment*, *303*, 114006. https://doi.org/10.1016/j.rse.2024.114006

Wieland, M., & Martinis, S. (2019). A modular processing chain for automated flood monitoring from multi-spectral satellite data. *Remote Sensing*, *11*(19), 2330. https://doi.org/10.3390/rs11192330

Wieland, M., Martinis, S., Kiefl, R., & Gstaiger, V. (2023). Semantic segmentation of water bodies in very high-resolution satellite and aerial images. *Remote Sensing of Environment*, *287*, 113452. https://doi.org/10.1016/j.rse.2023.113452

Williamson, A. G., Willis, I. C., Arnold, N. S., & Banwell, A. F. (2018). Controls on rapid supraglacial lake drainage in West Greenland: An exploratory data analysis approach. *Journal of Glaciology*, *64*(244), 208–226. https://doi.org/10.1017/jog.2018.8

Yang, K., Smith, L. C., Cooper, M. G., Pitcher, L. H., Van As, D., Lu, Y., et al. (2021). Seasonal evolution of supraglacial lakes and rivers on the southwest Greenland Ice Sheet. *Journal of Glaciology*, *67*(264), 592–602. https://doi.org/10.1017/jog.2021.10

Yang, K., Smith, L. C., Sole, A., Livingstone, S. J., Cheng, X., Chen, Z., & Li, M. (2019). Supraglacial rivers on the northwest Greenland Ice Sheet, Devon Ice Cap, and Barnes Ice Cap mapped using Sentinel-2 imagery. *International Journal of Applied Earth Observation and Geoinformation*, *78*, 1–13. https://doi.org/10.1016/j.jag.2019.01.008

Yuan, J., Chi, Z., Cheng, X., Zhang, T., Li, T., & Chen, Z. (2020). Automatic extraction of supraglacial Lakes in Southwest Greenland during the 2014–2018 melt seasons based on convolutional neural network. *Water*, *12*(3), 891. https://doi.org/10.3390/w12030891

Zhang, W., Yang, K., Smith, L. C., Wang, Y., Van As, D., Noël, B., et al. (2023). Pan-Greenland mapping of supraglacial rivers, lakes, and water-filled crevasses in a cool summer (2018) and a warm summer (2019). *Remote Sensing of Environment*, *297*, 113781. https://doi.org/10.1016/j.rse.2023.113781